Research Square

Preprints are preliminary reports that have not undergone peer review.
They should not be considered conclusive, used to inform clinical practice,
or referenced by the media as validated information.

Direct Imaging of Composition-driven Magnetoelastic Phase Transformations in Bulk Fe–Rh

Pedro Gorria

pgorria@uniovi.es

University of Oviedo https://orcid.org/0000-0002-1908-2953

Jiazhou Shen

Institut Laue Langevin (ILL) https://orcid.org/0000-0002-5908-4136

Kenny Padron-Aleman

Institut Laue Langevin (ILL)

Alessandro Tengattini

Institut Laue Langevin

Lukas Helfen

Institut Laue Langevin (ILL)

Gabriel Cuello

Institut Laue Langevin (ILL)

Jesus Blanco

University of Oviedo

José Sánchez-Llamasares

Instituto Potosino de Investigación Científica y Tecnológica A.C.

Pablo Alvarez-Alonso

University of Oviedo

Article

Keywords:

Posted Date: February 20th, 2026

DOI: https://doi.org/10.21203/rs.3.rs-8595400/v1

License: This work is licensed under a Creative Commons Attribution 4.0 International License.
Read Full License

Additional Declarations: There is **NO** Competing Interest.

Version of Record: A version of this preprint was published at Communications Materials on June 29th, 2026. See the published version at https://doi.org/10.1038/s43246-026-01251-5.

Direct Imaging of Composition-driven Magnetoelastic Phase Transformations in Bulk Fe–Rh

Author Information

Affiliations

Institut Laue-Langevin, Grenoble, France

K. Padrón-Alemán, J. Shen, A. Tengattini, L. Helfen & G.J. Cuello

Departamento de Física, Universidad de Oviedo, Oviedo, Spain

K. Padrón-Alemán, J.A. Blanco, P. Álvarez-Alonso & Pedro Gorria

University Grenoble Alpes, CNRS, Grenoble, France

A. Tengattini

Instituto Potosino de Investigación Científica y Tecnológica A.C., San Luis Potosí, México

J.L. Sánchez Llamazares

Instituto Universitario de Tecnología Industrial de Asturias, Universidad de Oviedo, Gijón, Spain

P. Álvarez-Alonso & Pedro Gorria

Contributions

K.P.-A. contributed to project formulation, beamtime proposal writing, neutron diffraction measurements, polarized neutron imaging experiments, data analysis, theoretical analysis, and manuscript writing. J.S. contributed to polarized neutron imaging experiments. A.T. contributed to project formulation and polarized neutron imaging experiments. L.H. contributed to polarized neutron imaging experiments. G.J.C. contributed to project formulation, neutron diffraction measurements, and polarized neutron imaging experiments. J.A.B. contributed to data analysis and theoretical analysis. J.L.S.Ll. contributed to sample fabrication and magnetization measurements. P.A.-A. contributed to data analysis, theoretical

analysis, and manuscript writing. P.G. contributed to project formulation, data analysis, and theoretical analysis. All authors contributed to manuscript final version and revision.

Corresponding author

Correspondence to: Pedro Gorria (pgorria@uniovi.es)

Abstract

Fe–Rh alloys exhibit world-leading multicaloric responses associated with a magnetoelastic first-order magnetic phase transition between antiferromagnetic (AFM) and ferromagnetic (FM) states. Here, we demonstrate that polarized neutron imaging provides a powerful technique to deciphering the fundamental mechanisms governing the phase transformation in bulk $Fe_{100-x}Rh_x$ alloys (x = 50, 51, and 52 at.%) by resolving the three-dimensional spatial pathways, and magnetic domain coexistance. Despite identical synthesis route, near-equiatomic $Fe_{100-x}Rh_x$ alloys exhibit markedly different transition temperatures and transition temperature widths upon small variations in Rh content. Polarized neutron-contrast radiography reveal that the equiatomic alloy undergoes a strongly heterogeneous transformation, characterized by the extended coexistence of AFM and FM domains over broad temperature ranges and spatially distributed local transition temperatures. This behaviour is accompanied by multiple, spatially separated nucleation-and-growth regimes, consistent with a defect-mediated transformation mechanism. In contrast, Rh-rich compositions exhibit a more uniform and abrupt magnetic transition, with reduced AFM–FM coexistence, indicating that excess Rh acts as an effective nucleation catalyst that homogenizes the phase transformation across the entire alloy volume. These results expose the hidden composition-driven control of AFM–FM phase coexistence and transformation pathways in Fe–Rh, and establish polarized neutron imaging as a unique mesoscale probe of magnetoelastic phase transformations in bulk functional magnetic materials.

Introduction

Magnetic materials can be explored across three complementary length scales: the microscopic regime, encompassing atomic structure and spectroscopy; the mesoscopic regime, involving magnetic domains, Néel walls, Bloch points, and other topological or structural magnetic defects; and the macroscopic regime, characterized by magnetization curves and bulk magnetic phases. While most neutron- and X-ray-based studies focus on the microscopic scale using techniques such as neutron diffraction, magnetic X-ray diffraction, and dichroism, these probes also offer unique access to the mesoscopic regime, enabling the investigation of three-dimensional magnetic inhomogeneities and defects that disrupt the periodic magnetic lattice. Owing to the weak interaction between neutrons and matter—arising from their electrical neutrality—neutrons penetrate deeply and non-destructively into materials, ensuring that the measured information is minimally perturbed by the probe itself and, in some cases, inaccessible by other experimental techniques. In particular, this property of neutrons enables two-dimensional (radiography) and three-dimensional (tomography) neutron imaging investigations of the bulk interior of materials[1–3]. Futhermore, the intrinsic magnetic moment of neutrons provides sensitivity to internal magnetic fields and magnetic moments within the samples. Consequently, polarized neutron imaging (PNI) is particularly well suited for the study of functional magnetic materials, as it enables direct visualization of magnetic phase transitions, magnetic domain evolution, and mesoscale magnetic inhomogeneities within bulk samples[4–7].

When a polarized neutron beam traverses a ferromagnetic (FM) material with randomly oriented magnetic domains, spin precession in the internal magnetic fields and spin-flip magnetic scattering progressively depolarize the beam[8]. Consequently, an analyzer placed downstream transmits only the neutrons polarized along the selected analysing axis, leading to a strong reduction and increased statistical asymmetry in the detected intensities of oppositely polarized neutron states[1,2]. In contrast, when the beam passes through an antiferromagnetic (AFM) material—where individual domains possess no net magnetization and magnetic scattering is weaker—the neutron polarization is largely preserved. In this

case, the analyzer efficiently transmits the beam, yielding a near-maximum detected intensity for the matching incident polarization, or strong attenuation for the opposite polarization[9,10]. As a result, during AFM↔FM phase transitions the transmitted neutron intensity directly encodes the local magnetic state of the material. This generates a spatially resolved contrast that enables quantitative identification and mapping of coexisting FM and AFM regions throughout the bulk of the sample.

In imaging, the radiographic contrast is governed by the beam's depolarization ratio, $-1 \leq P/P_0 \leq 1$, where P_0 and P denote the neutron beam polarizations before and after traversing the sample. Negative values correspond to neutron spin rotation exceeding $\pi/2$, which occurs in regions with sufficiently strong local magnetic fields[2]. The beam polarization is expressed as[1]:

$$P = \frac{I_\uparrow - I_\downarrow}{I_\uparrow + I_\downarrow} \quad (1),$$

where $I_\uparrow$ and $I_\downarrow$ denote transmitted intensities for spin up (↑) and spin down (↓) neutrons, respectively. While P reflects magnetic-field-induced spin rotations, the sample transmission:

$$\frac{I}{I_0} = \frac{I_\uparrow + I_\downarrow}{I_{0\uparrow} + I_{0\downarrow}} \quad (2)$$

measures the intensity attenuation due to the nuclear neutron absorption and scattering, thus is insensitive to magnetic effects.

In this work, we exploit the unique capabilities of PNI to resolve the spatial distribution of magnetic phases and the phase-conversion mechanisms governing the AFM↔FM transition in bulk equiatomic and nearly-equiatomic (with a small excess of Rh) Fe–Rh alloys giving rise to different transformation behaviours. Central to these magnetoelastic transitions is the nucleation and growth of regions during the transformation. Such processes may proceed either uniformly throughout the material or preferentially at specific sites linked to chemical inhomogeneities, antisite disorder, or microstructural defects such as twinning and dislocations. Once incipient magnetic domains have formed, their subsequent growth depends on various factors, including diffusion kinetics, temperature, interface mobility, the presence of secondary phases, and microstructural defects. Variations in the relative importance of these factors can

lead to a broad or narrow distribution of local transition temperatures, reflecting the degree of heterogeneity in the transformation process [11–13]. This intrincate interplay among magnetic, structural, and microstructural degrees of freedom makes understanding domain nucleation and growth across the phase transition essential in materials whose functional response arises from magnetostructural coupling.

Arising from magnetostructural coupling, Fe–Rh alloys provide a benchmark system, exhibiting a first-order magnetic phase transition (FOMPT) between low-temperature AFM and high-temperature FM states, accompanied by a ~1 % volume expansion of the cubic B2 (CsCl-type) crystal structure without any change in symmetry [14–21]. Importantly, the spatial distribution of coexisting AFM and FM phases during this magnetoelastic transformation[15,21–24] strongly influences the characteristics of the transition and, consequently, the associated functional properties, including giant magnetocaloric[19], barocaloric[25], and elastocaloric[26] responses. Notably, previous studies report discrepancies in how near-equiatomic compositions traverse the phase transition, highlighting the strong dependence of the transformation pathway on composition[21,23,27,28], synthesis method and specific synthesis parameters[15,29–31], and microstructure[22]. To probe how these factors influence magnetic phase nucleation and growth, advanced X-ray imaging approaches, including nano X-ray diffraction and X-ray magnetic circular dichroism combined with photoemission electron microscopy, have been used[13,32]. However, their intrinsic surface sensitivity confines these approaches to thin films, leaving the spatial pathways and mechanisms of bulk-phase transformations largely unresolved.

In this work, we continuously monitor the spatial coexistence of AFM and FM regions throughout the magnetic phase transition in three bulk $Fe_{100-x}Rh_x$ alloys with x = 50, 51, and 52 using neutron polarization contrast imaging. By isolating composition as the key parameter governing the transformation pathway in bulk Fe–Rh, we elucidate the influence of subtle variations in Rh content on phase-nucleation and growth processes. To the best of our knowledge, the results provide the first direct visualization of how the magnetoelastic phase transition in bulk Fe–Rh alloys evolves, establishing a basis for composition-guided design of caloric materials.

Results

Phase transformation

Neutron diffraction experiments confirm that all three Fe–Rh alloys investigated adopt the B2 (CsCl-type) crystallographic structure and exhibit AFM order at room temperature (RT). Detailed diffraction data for the $Fe_{50}Rh_{50}$ and $Fe_{49}Rh_{51}$ alloys are reported in[16,33], while that for $Fe_{48}Rh_{52}$ is provided in the **Supplementary Information** (see **Fig. S1 S2**). Isofield magnetization curves measured under 5 mT, normalized as $M(T)/M^{max}$ (to facilitate their comparison) reveal a systematic decrease in the transition temperature with increasing Rh content (**Fig. 1a**), thus favoring the stabilization of the FM state. In addition, magnetization curves measured at 2 T and similarly normalized emphasize pronounced differences in the magnetization evolution across the three compositions (**Fig. 1b**), clearly highlighting variations in both the magnetization jump and the thermal hysteresis, ΔT_{hyst}, associated with the AFM↔FM phase transition. Although no simple monotonic correlation between composition and hysteresis width is observed, the off-equiatomic alloys exhibit systematically smaller thermal hysteresis than the equiatomic composition. The temperature interval required to complete the AFM→FM transformation, defined as the difference between the end (AF_f) and the start (AF_S) temperatures of the transition determined from the $M(T)^{2T}$ data during heating, differs markedly among the alloys (33 K for $Fe_{50}Rh_{50}$, 1 K in $Fe_{49}Rh_{51}$, and 6 K in $Fe_{48}Rh_{52}$, as determined by means of the tangent method). Similarly, the reverse FM→AFM shows distinct abruptness and progression among the three alloys. The temperature intervals between the start (FA_S) and finish (FA_f) temperatures amount to 35 K, 2 K, and 5 K for $Fe_{50}Rh_{50}$, $Fe_{49}Rh_{51}$, and $Fe_{48}Rh_{52}$, respectively. This further highlights that the distinct evolution of the AFM↔FM phase transition among the three alloys depends strongly on their composition. The key parameters that characterize the phase transition are summarized and described in the **Supplementary Information** (see **Table S1**).

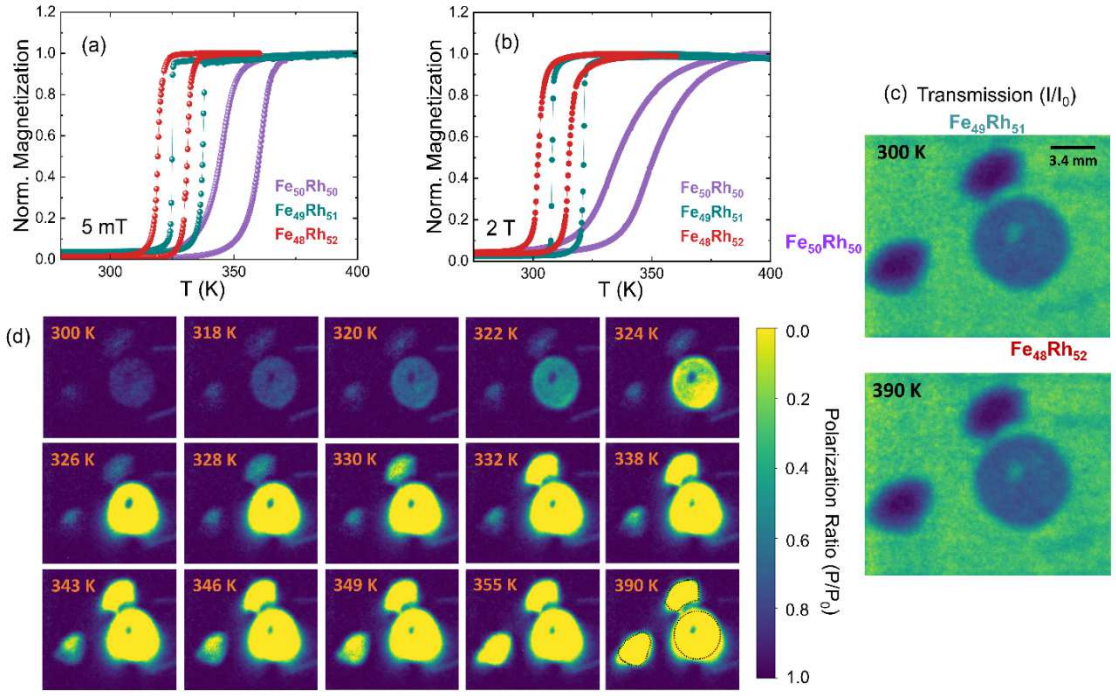


Fig. 1. AFM–FM phase evolution in bulk Fe–Rh alloys. a, b Temperature dependence of the normalized magnetization measured under applied magnetic field of 5 mT and 2 T for $Fe_{50}Rh_{50}$, $Fe_{49}Rh_{51}$, and $Fe_{48}Rh_{52}$ alloys. **c** Typical neutron transmission radiographs of the FOV at two selected temperatures, showing the position and outline of the three samples. Sample locations remain fixed throughout all measurements: top ($Fe_{49}Rh_{51}$), bottom right ($Fe_{48}Rh_{52}$), and bottom left ($Fe_{50}Rh_{50}$). **d** Depolarization-contrast radiographs resolving the AFM→FM phase transition in equiatomic and near-equiatomic Fe–Rh alloys, obtained using the neutron polarized imaging technique. Black dashed lines at the 390 K image represent the actual sample silhouette reconstructed from transmission images. Full heating and cooling sequences for all samples are provided as radiographs and videos in the **Supplementary Information**. The hollow observed in $Fe_{48}Rh_{52}$ is an intrinsic feature related to the synthesis process and not an experimental artifact.

To directly visualize the phase evolution throughout the bulk, PNI measurements were performed on the three samples placed simultaneously within the whole Field-of-View (FOV) provided by the PNI set-up. **Fig. 1c** shows representative neutron transmission radiographs collected at two selected temperatures,

158 corresponding to the fully AFM state and to the state after completion of the transformation into the FM
159 phase. The outlines and positions of the specimens remain mostly unchanged throughout the transition,
160 providing a clear geometrical reference. A small but negligible displacement (approximately 1~2 pixels),
161 predominantly along the vertical direction, is observed and arises from the thermal expansion of the
162 aluminum sample holder. This stable baseline enables unambiguous interpretation of the subsequent
163 magnetic contrast. **Fig. 1d** illustrates the corresponding polarization-ratio radiographs acquired during
164 heating across the AFM-to-FM magnetoelastic phase transition. Although the spatial resolution is larger
165 than the typical Fe–Rh magnetic domain size (FM domain width of ~1 μm reported in thin films)[34], the
166 pixel size remains sufficiently small to resolve and quantitatively map the depolarization contrast and its
167 variation throughout the entire sample volume, thus enabling unambiguous tracking of the transformation
168 progression. PNI measurements thus provide a direct and comparative view of the phase transformation
169 among the different compositions. In particular, the rather broad magnetic transition for $Fe_{50}Rh_{50}$ is
170 clearly observed in **Fig. 1d** and **Fig. S2** in the **Supplementary Information**. The earliest signatures of
171 transformation appear at 322 K, where a localized region exhibits a slight increase in depolarization
172 contrast while the rest of the sample remains unchanged, indicating the onset of FM nucleation in
173 spatially distinct regions. This suggests that certain areas of the material begin transforming from the
174 AFM to the FM state earlier than others. With increasing temperature, this region intensifies and expands
175 as the FM phase progressively grows and spreads throughout the sample volume. By approximately 355
176 K, the beam is fully depolarized within the sample, indicating either that the transformation to the FM
177 phase is complete or that the FM fraction has become sufficiently large to fully depolarize the neutron
178 beam.

179 Conversely, the phase transformation in $Fe_{49}Rh_{51}$ and $Fe_{48}Rh_{52}$ progresses more homogeneously across
180 the sample volume. For $Fe_{49}Rh_{51}$, the first detectable depolarization changes appear at approximately 326
181 K, manifested as a brighter region near the centre of the sample. With increasing temperature, the
182 depolarization contrast in this region intensifies, while the surrounding areas undergo a slower and more

gradual depolarization, until complete beam depolarization is reached at ~332 K. A similar behavior is observed in $Fe_{48}Rh_{52}$, where earlier depolarization changes appear around 320 K, and are distributed almost uniformly across the entire sample. With increasing temperature, the depolarization contrast progressively intensifies until the neutron beam becomes fully depolarized at approximately 326 K. Analogous spatial features are observed during the reverse FM→AFM transition upon cooling in all three alloys (see **Fig. S3** in the **Supplementary Information**).

Averaging the polarization ratio over the entire sample volume provides a quantitative description of the phase transformation. **Fig. 2a-c** show the temperature dependence of the mean depolarization ratio for each alloy during heating and cooling. The reduction in polarization upon heating reflects an increasing fraction of the material being transformed into the FM phase; conversely, recovery of polarization during cooling marks the reappearance of the AFM phase. The resulting curves closely mimic the $M(T)$ curves: the $Fe_{50}Rh_{50}$ alloy exhibits a broad transformation, whereas the Rh-rich compositions present sharp transitions, together with the characteristic thermal hysteresis of the FOMPT (see **Fig. S4** of the **Supplementary Information**, where the evolution of $(1 - P/P_0)$ as a function of temperature is compared with the $M(T)$ curves. The starting temperatures for the AFM→FM transition are approximately 333 K, 327 K, and 320 K for the $Fe_{50}Rh_{50}$, $Fe_{49}Rh_{51}$, and $Fe_{48}Rh_{52}$ samples, respectively. Minor differences between these values and those derived from low-field magnetization measurements likely reflect intrinsic differences between the techniques, as well as variations in experimental configuration and temperature-sweep rates. It is worth noting that the depolarization curves drop to ~ 0 at temperatures above AF_S, reflecting the growth and coalescence of FM regions that strongly enhance beam depolarization. Conversely, the polarization ratio does not reach $P/P_0 = 1$ at low temperatures. This behaviour is most likely attributable to the high sensitivity of polarized neutrons to localized magnetic components, such as those present at magnetic domain boundaries[8], rather than to the persistence of residual FM phase fractions. Once the phase transition is complete, the heating and cooling branches

overlap, in agreement with previous neutron thermo-diffraction studies that have not reported evidence of FM order in this temperature regime[16].

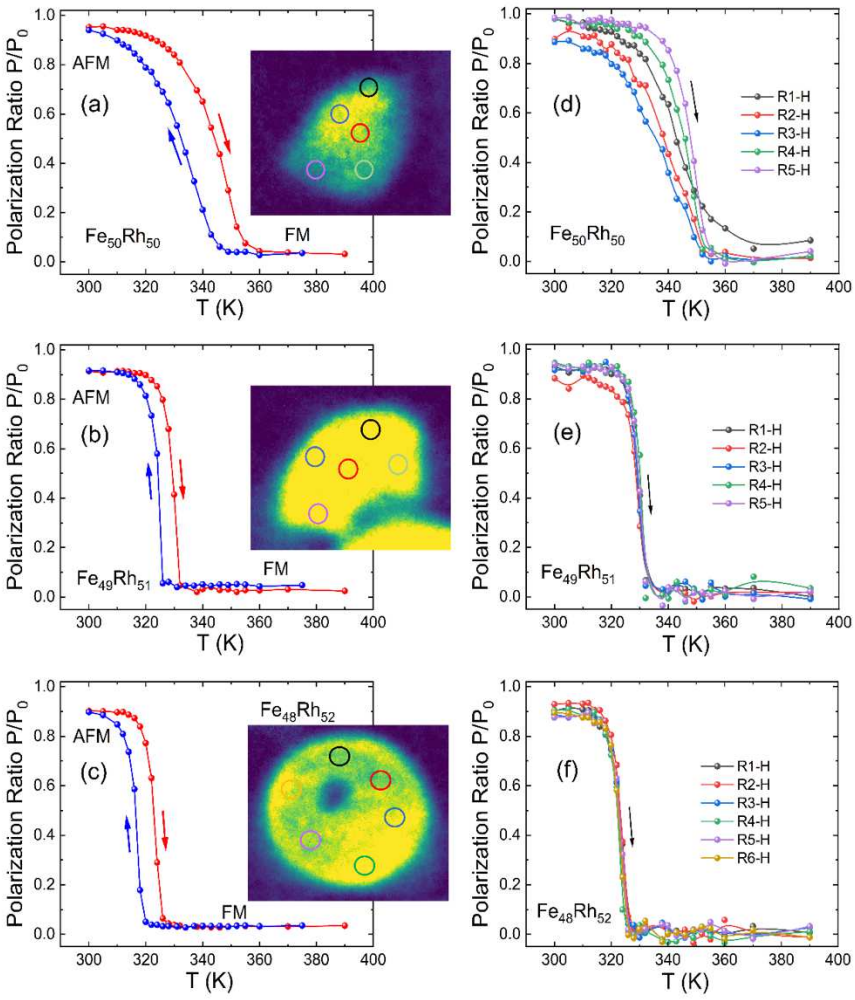


Fig. 2. Temperature-dependent averaged depolarization ratio. Temperature dependence of the averaged depolarization ratio over the full FOV of **a** $Fe_{50}Rh_{50}$, **b** $Fe_{49}Rh_{51}$, and **c** $Fe_{48}Rh_{52}$ samples. Red and blue arrows indicate heating and cooling, respectively. Evolution of the depolarization ratio during heating calculated from selected areas within the samples for **d** $Fe_{50}Rh_{50}$, **e** $Fe_{49}Rh_{51}$, and **f** $Fe_{48}Rh_{52}$. The black arrows indicate the direction of the temperature change. Each area corresponds to a circular region with a diameter of 10 pixels (≈ 570 μm). The accompanying images in **a**, **b**, and **c** illustrate the selected regions within the samples (circled).

To assess the uniformity of the AFM↔FM phase transition in the three alloys, we examined the depolarization ratio across different regions within each sample. **Fig. 2d–f** present the temperature dependence of the depolarization ratio for selected circular regions with a diameter of 10-pixel (approximately 570 μm) for the three samples. The corresponding cooling data are depicted in **Fig. S5** of the **Supplementary Information**. For $Fe_{50}Rh_{50}$ (**Fig. 2d**), the curves reveal pronounced variations across different regions: each region undergoes the AFM↔FM transformation over a broad range of transition temperatures and with varying transition temperature widths. This marked inhomogeneous behavior reflects an extensive coexistence of AFM and FM phases throughout the bulk, consistent with the T-FORC analysis of $Fe_{50}Rh_{50}$, which suggests a defect-driven transformation mechanism[23]. In contrast, the near-equiatomic samples (**Fig. 2e–f**) display an almost uniform transformation across all selected regions, with only minor local variations, likely caused by residual microstructural defects[12]. These findings suggest that the distinct transformation characteristics of the three alloys arise primarily from subtle compositional differences, despite identical fabrication procedures and thermal treatment conditions. Notably, the current analysis supports the hypotheses regarding the role of the extra Rh atoms: the higher Rh content in the off-equiatomic samples likely acts as point defects and nucleation centers, promoting a more uniform phase evolution[23]. This effect is linked to subtle changes in the local Fe environment: while Fe atoms in the equiatomic alloy occupy a well-ordered B2 lattice, in off-equiatomic compositions the increase of local disorder tends toward an A2-like lattice configuration.

Discussion

Polarized neutron imaging technique enabled, for the first time, direct visualization of the evolution of the first-order magnetoelastic phase transition in bulk Fe–Rh alloys via 2D radiographs. The temperature depedence of the average polarization contrast across the entire sample reproduces the features observed in the magnetization curves, revealing a broad transformation in the $Fe_{50}Rh_{50}$ alloy and a sharp transition in the off-equiatomic Rh-rich compositions. In $Fe_{50}Rh_{50}$, distinct transformation pathways emerge across different regions of the sample, demonstrating that various areas undergo the AFM↔FM transformation

at different temperatures as it can be observed in **Fig. 3**. These findings demonstrate a heterogeneous transformation throughout the sample volume and provide direct evidence that nucleation and growth occur simultaneously within the same temperature range, in agreement with the defect-driven mechanism previously inferred from T-FORC analysis[23]. In contrast, the $Fe_{49}Rh_{51}$ and $Fe_{48}Rh_{52}$ alloys exhibit a homogeneous, spatially uniform transformation that occurs over a narrow temperature range that shifts to lower transition temperatures as Rh content increases. This behavior supports the hypothesis that the additional Rh atoms act as effective nucleation centers, promoting uniform nucleation throughout the bulk.

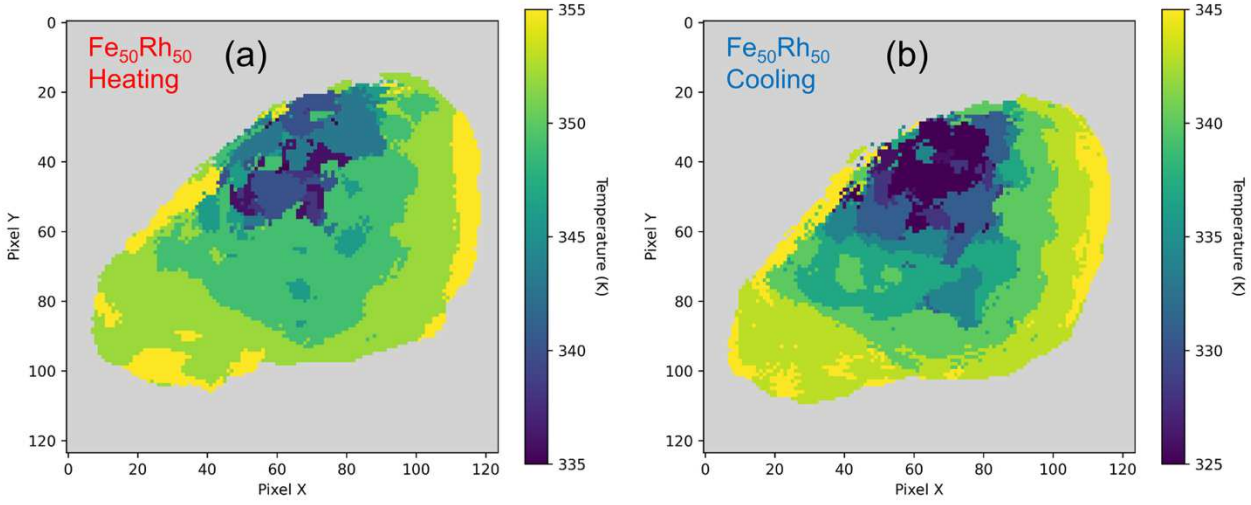


Fig. 3. $Fe_{50}Rh_{50}$ T_t map. Transition temperature distribution over the total FOV of the sample $Fe_{50}Rh_{50}$ in (a) heating and (b) cooling regimes. Each value of T_t [in this case defined as the minimum of $d(P/P_0)/dT$] is determined independently from the temperature dependence of the neutron depolarization ratio of each pixel.

Overall, this work demonstrates that even minor compositional deviations significantly influence the magnetoelastic phase transition in induction-melted bulk Fe–Rh alloys. A small increase in Rh concentration modify the balance between nucleation and growth, thereby controlling the transition temperature range, the width of the thermal hysteresis, and the spatial uniformity of the transformation.

In conclusion, this work provides direct insight into the transformation mechanisms of bulk alloys undergoing first-order phase transitions—phenomena previously accessible only through indirect measurements—and establishes polarized neutron imaging as a uniquely powerful tool for resolving mesoscale phase evolution in bulk magnetic materials. These findings highlight the critical role of subtle compositional variations in dictating nucleation and growth dynamics, offering a pathway to rationally tailor phase-transition characteristics through alloy design. Beyond Fe–Rh, the methodology introduced here opens new opportunities to investigate other first-order transitions where local disorder, microstructure, or processing history strongly influence functional properties. Looking forward, extending polarized neutron imaging to dynamic conditions under external stimuli—such as pressure, or strain—will enable unprecedented insights into phase stability and transformation kinetics, advancing the design of next-generation magnetic multifunctional materials.

Methods

Sample synthesis

Binary $Fe_{100-x}Rh_x$ (x = 50, 51, and 52 at.%) alloys were synthesized from high-purity iron (99.98 % pure) and rhodium (99.95 % pure) following a multistep procedure: (i) pre-alloying using the conventional arc-melting technique, (ii) subsequent induction melting, (iii) thermal treatment, and (iv) fast quenching in iced-water. Details of the preparation process are described elsewhere[21].

Magnetic measurements

Magnetization measurements were performed using the vibrating sample magnetometer (VSM) option of a Quantum Design PPMS® Dynacool®-9T system in the temperature range from 290 K to 400 K under applied magnetic field values of 5 mT and 2 T at a temperature sweeping rate of 1 K/min.

Polarized neutron imaging

Polarized neutron imaging experiments were performed at the MoTo instrument of the Institut Laue-Langevin (Grenoble, FR) to extract depolarization-contrast at a wavelength of 2.4 Å. The neutron detector used in the experiment consists of a 100 μm thick LiF neutron scintillator paired with an optical system that includes a reflecting mirror and lenses for photon collection and a Hamamatsu® Orca®-Flash4.0 CMOS camera with a 2048 × 2048 pixel array used to capture the optical images. The used FOV in the setup is 117 × 117 mm^2, corresponding to an effective pixel size of ~57 μm. The pinhole geometry of the beam defines the collimation and enables spatially resolved measurements. For polarized-neutron imaging at ILL[35], solid-state benders[36] serve as polarizer and analyzer with around 90 % beam polarization across the region-of-interest (ROI) while a Mezei spin flipper allows for reversal of the beam polarization. The analyzer stray magnetic field has a maximum at the sample position of 2 mT. The sample is mounted on a rotation stage, enabling the acquisition of images at multiple projection angles; it is is located about 4.5 m

downstream of the second aperture. The sample stage allows translation of approximately 500 mm along the beam axis relative to the movable neutron detector. Transmission radiographs are recorded using the detector system described above.

Three bulk samples with nominal compositions $Fe_{50}Rh_{50}$, $Fe_{49}Rh_{51}$, and $Fe_{48}Rh_{52}$ were measured simultaneously. A home-built sample holder and temperature-control system were designed for the experiment. The samples were mounted on an aluminium block, which served as both a mechanical holder and a heat-transfer element; they were sealed in a Teflon cylinder to reduce the temperature gradient. A commercial hot plate (Miniware MHP-50), together with two Type-K thermocouples and a PID controller, were used to heat up the sample from the bottom of the aluminium holder and keep the temperature stable during the measurement.

Depolarization-contrast radiographs were acquired at various temperatures during both heating and cooling regimes, covering the full AFM↔FM magnetoelastic phase transition in the three samples. Each radiograph consisted of 13 frames in the spin-up configuration and 27 frames in the spin-down configuration, with an acquisition time of 30 s per frame. All radiographs were post-processed to reduce noise by subtracting the electronic dark-current noise from the CMOS camera and were normalized to flat-field images where only the neutron aperture and the detector are present. Depolarization contrast is normalized on a pixel-by-pixel basis using a reference measurement in which the spin polarizer, analyzer, and flippers are in place, but with the sample setup removed from the FOV.

Data Availability

The main data supporting the findings of this study are available within the paper and its Supplementary Information. Neutron diffraction and imaging data have been made available free of charge from ILL under the identifiers DOI: 10.5291/ILL-DATA.EASY-1560 and DOI: 10.5291/ILL-DATA.1-05-165. Other data are available from the corresponding author upon request.

References

1. Strobl, M. *et al.* Polarization measurements in neutron imaging. *J. Phys. D: Appl. Phys.* **52**, 123001 (2019).

2. Kardjilov, N., Hilger, A., Manke, I., Strobl, M. & Banhart, J. Imaging with Polarized Neutrons. *J. Imaging* **4**, 23 (2018).

3. *Neutron Imaging and Applications: A Reference for the Imaging Community*. (Springer, New York, 2009).

4. Schulz, M. *et al.* Towards a tomographic reconstruction of neutron depolarization data. *J. Phys.: Conf. Ser.* **211**, 012025 (2010).

5. Busi, M. *et al.* Polarization contrast neutron imaging of magnetic crystallographic phases. *Mater. Today Adv.* **16**, 100302 (2022).

6. Busi, M. *et al.* 3D characterization of magnetic phases through neutron polarization contrast tomography. *Addit. Manuf. Lett.* **6**, 100155 (2023).

7. Schulz, M., Neubauer, A., Böni, P. & Pfleiderer, C. Neutron depolarization imaging of the hydrostatic pressure dependence of inhomogeneous ferromagnets. *Appl. Phys. Lett.* **108**, 202402 (2016).

8. Mühlbauer, S. *et al.* Magnetic small-angle neutron scattering. *Rev. Mod. Phys.* **91**, 015004 (2019).

9. Oji, U. K. *et al.* Polarized neutron imaging at NeXT (neutron and x-ray tomograph) at Institut Laue Langevin. *Rev. Sci. Instrum.* **95**, 063703 (2024).

10. Quan, Y. *et al.* Impact of the neutron-depolarization effect on polarized neutron scattering in ferromagnets. *IUCrJ* **8**, 455–461 (2021).

11. Christian, J. W. *The Theory of Transformations in Metals and Alloys*. (Pergamon Press, Amsterdam, 2002).

12. Zhang, X. *et al.* Defect-characterized phase transition kinetics. *Appl. Phys. Rev.* **9**, 041311 (2022).

13. Keavney, D. J. *et al.* Phase Coexistence and Kinetic Arrest in the Magnetostructural Transition of the Ordered Alloy FeRh. *Sci. Rep.* **8**, 1778 (2018).

14. Zakharov, A., Antonina M. Kadomtseva, R. Z. Levitin and E. G. Ponyatovskiĭ. Magnetic and magnetoelastic properties of a metamagnetic iron-rhodium alloy. *J. Exptl. Theoret. Phys.* **46**, 1348–1353 (1964).

15. Sánchez-Valdés, C. F. *et al.* The effect of cooling rate on magnetothermal properties of Fe49Rh51. *J. Magn. Magn. Mater.* **498**, 166130 (2020).

16. Padrón-Alemán, K. *et al.* Scrutinizing the sharp magnetoelastic transition and kinetic arrest in $Fe_{49}Rh_{51}$ alloy using neutron thermo-diffraction. *J. Mater. Chem. C* **13**, 7017–7026 (2025).

17. Bertaut, E. F. *et al.* Magnetic Structure Work at the Nuclear Center of Grenoble. *J. Appl. Phys.* **33**, 1123–1124 (1962).

18. Shirane, G., Chen, C. W., Flinn, P. A. & Nathans, R. Mössbauer Study of Hyperfine Fields and Isomer Shifts in the Fe-Rh Alloys. *Phys. Rev.* **131**, 183–190 (1963).

19. Nikitin, S. A. *et al.* The magnetocaloric effect in Fe49Rh51 compound. *Phys. Lett. A* **148**, 363–366 (1990).

20. Chirkova, A. *et al.* Giant adiabatic temperature change in FeRh alloys evidenced by direct measurements under cyclic conditions. *Acta Mater.* **106**, 15–21 (2016).

21. Arreguín-Hernández, M. L. *et al.* Magnetoelastic transition and magnetocaloric effect in induction melted Fe100−xRhx bulk alloys with x = 50, 51. *J. Alloys Compd.* **871**, 159586 (2021).

22. Chirkova, A. *et al.* The effect of the microstructure on the antiferromagnetic to ferromagnetic transition in FeRh alloys. *Acta Mater.* **131**, 31–38 (2017).

23. Padrón-Alemán, K. *et al.* Study of the magnetoelastic phase transition in near equiatomic FeRh alloys through T-FORC analysis and neutron diffraction. *J. Alloys Compd.* **1010**, 177876 (2025).

24. Zverev, V. I. *et al.* Influence of structural defects on the magnetocaloric effect in the vicinity of the first order magnetic transition in Fe50.4Rh49.6. *Appl. Phys. Lett.* **108**, 192405 (2016).

25. Stern-Taulats, E. *et al.* Barocaloric and magnetocaloric effects in Fe49Rh51. *Phys. Rev. B* **89**, 214105 (2014).

26. Nikitin, S. A. *et al.* Giant elastocaloric effect in FeRh alloy. *Phys. Lett. A* **171**, 234–236 (1992).

27. Rumiantsev, E. *et al.* Doping position estimation for FeRh-based alloys. *Sci. Rep.* **14**, 20612 (2024).

28. Zverev, V. I. *et al.* Peculiarities of the phase transformation dynamics in bulk FeRh based alloys from magnetic and structural measurements. *J. Magn. Magn. Mater.* **522**, 167560 (2021).

29. Lommel, J. M. & Kouvel, J. S. Effects of Mechanical and Thermal Treatment on the Structure and Magnetic Transitions in FeRh. *J. Appl. Phys.* **38**, 1263–1264 (1967).

30. Kushwaha, P., Lakhani, A., Rawat, R. & Chaddah, P. Influence of thermal annealing and magnetic field on first order magnetic transition in Pd substituted FeRh. *J. Phys.: Conf. Ser.* **200**, 032038 (2010).

31. Rodionov, V. *et al.* Thermal Hysteresis Control in Fe49Rh51 Alloy through Annealing Process. *Processes* **9**, 772 (2021).

32. Baldasseroni, C. *et al.* Temperature-driven nucleation of ferromagnetic domains in FeRh thin films. *Appl. Phys. Lett.* **100**, 262401 (2012).

33. Padrón-Alemán, K., Arreguín-Hernández, M. L., Cuello, G. J., Alvarez-Alonso, P. & Sánchez Llamazares, J. L. Phase analysis of near equiatomic bulk FeRh alloys: X-ray versus neutron diffraction and magnetization measurements. *Mater. Chem. Phys.* **327**, 129904 (2024).

34. Temple, R. C. *et al.* Antiferromagnetic-ferromagnetic phase domain development in nanopatterned FeRh islands. *Phys. Rev. Materials* **2**, 104406 (2018).

35. Oji, U. K., Tengattini, A., Helfen, L., Manke, I., Cubitt, R. & Kardjilov, N. Polarized neutron imaging at NeXT (neutron and x-ray tomograph) at Institut Laue Langevin. *Rev. Sci. Instrum.* **95**, 063703 (2024).

36. Krist, T. H., Kennedy, S. J., Hicks, T. J. & Mezei, F. New compact neutron polarizer. *Physica B* **241-243**, 82 (1997).

Acknowledgements

Work partially supported by the following projects: (a) PTDC/EMETED/3099/2020, UIDP/04968/2020-Programático, from CONAHCyT; (b) PID2022-138256NB-C21, from Spanish MCIN/AEI/10.13039/501100011033 and ERDF, EU; (c) GRU-GIC-24-113, from SEKUENS (Principality of Asturias); (d) CF-2023-I-2143 from SECIHTI, Mexico. The support received from Laboratorio Nacional de Nanociencias y Nanotecnología (LINAN, IPICyT) is gratefully acknowledged. K. Padrón-Alemán acknowledges the Institute Laue-Langevin for his PhD/CFR contract (Reference: ESP-5-2023). Authors acknowledge the Institute Laue-Langevin for the beam-time allocation 5-31-2945 (MoTo) and EASY-1560 (D1B), and Dr. Vivian Nassif for technical support during the experiments at D1B instrument.

Ethics declarations

Competing interests

The authors declare no competing interests.

Supplementary Files

This is a list of supplementary files associated with this preprint. Click to download.

- SuppInfoPadronAlemanetal.pdf
- VideoPadronAlemanetal.mp4